Supplementary Information

A topological Hund nodal line antiferromagnet

Xian P. Yang et al.

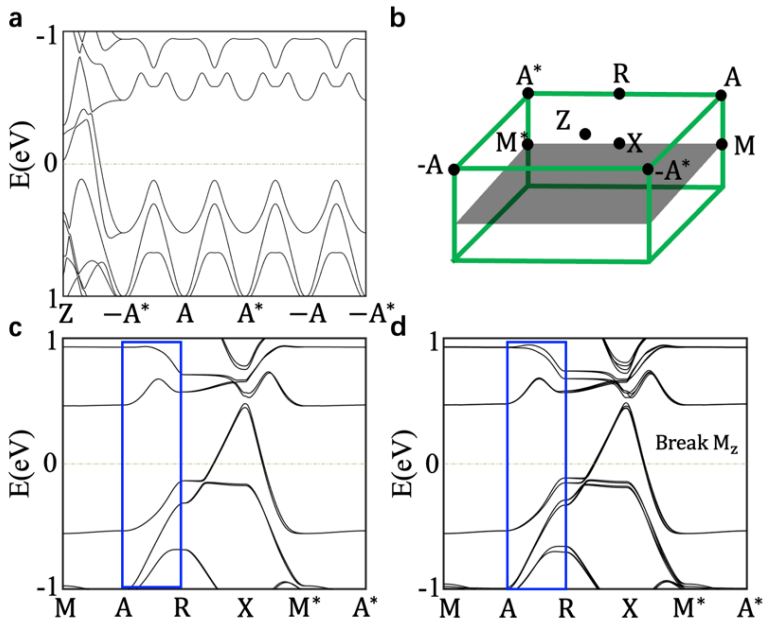

Supplementary Fig. 1. Calculated bulk electronic band structure along the boundary of the Brillouin zone with spin-orbit coupling and magnetism included. a, DFT calculations of the fourfold degenerate AFM nodal line on the Z-R-A plane. The nodal line forms a closed loop along the boundary of the Brillouin zone (BZ) on the Z-R-A plane. **b,** Bulk BZ of YMn_2Ge_2 with high symmetry points marked. The magnetic nodal line around the boundary of the 3D BZ is indicated by the green lines. **c,** DFT calculations of the fourfold nodal line on the M-A-X-R high symmetry plane. Fourfold bands exist only along the boundary of the BZ, consistent with our symmetry analysis. **d,** If M_z mirror symmetry is broken, the fourfold nodal line would split into two branches, highlighted by the blue rectangle. This demonstrates how mirror symmetry protects the AFM nodal line.

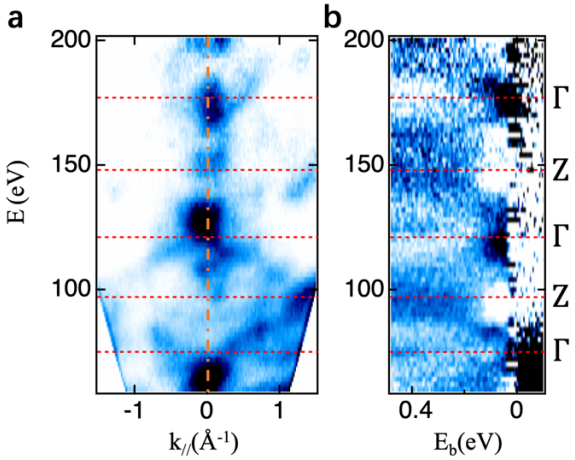

Supplementary Fig. 2. Photon energy dependence along the k_z direction. a, Photon energy dependence of cut 1 in Fig. 1 from 60 to 200 eV. **b,** ARPES dispersion along the orange dashed line in **a**. Red dashed lines indicate the positions of the high symmetry points along the k_z axis. Periodic patterns can be seen in the photon energy scan, and photon energies of 148 and 97 eV correspond to the Z-A-R high symmetry plane.

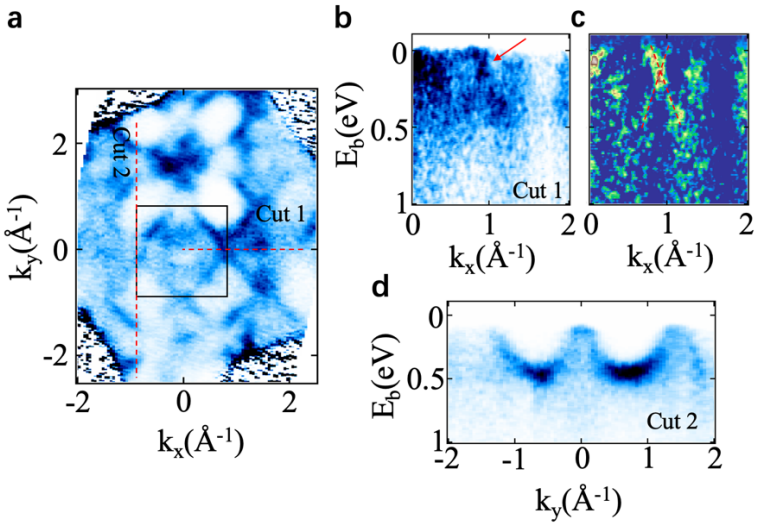

Supplementary Fig. 3. Soft X-ray ARPES on the AFM nodal line. a, ARPES Fermi surface spectrum on the (001) surface taken with incident photon energy of 552 eV corresponding to the A-Z-R high symmetry plane. The black box represents the Brillouin zone. Red dashed lines indicate the positions of cuts 1 and 2. **b,** ARPES dispersion along Z-R direction demonstrating the Dirac crossing at the R point (marked by the red arrow). **c,** Corresponding second curvature plot of **b**. Red dotted lines are a guide for the eye. **d,** ARPES dispersion along A-R direction demonstrating the Dirac nodal line. The bulk sensitive ARPES data confirm the bulk origin of the Dirac cone and the nodal line shown in Fig. 1.

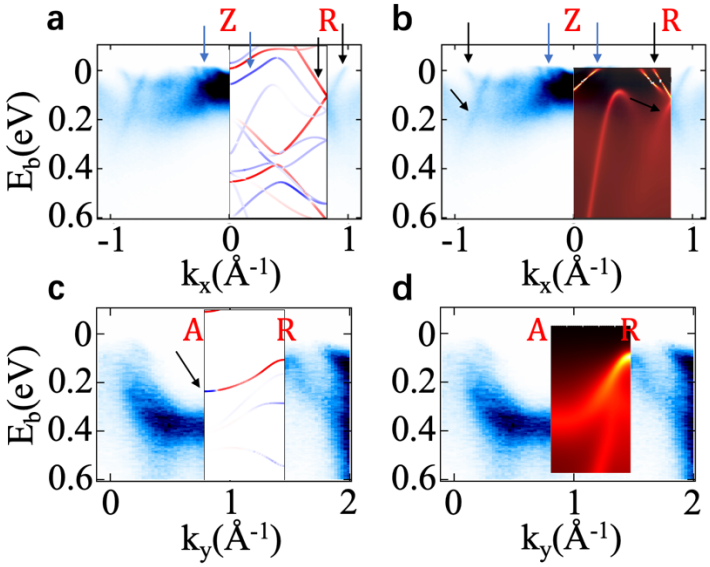

Supplementary Fig. 4. Comparison between ARPES and calculations. a, ARPES dispersion along Z-R direction. Same as Fig. 1**g** or cut 2 in Fig. 1. DFT calculations are superimposed on ARPES to illustrate the overall agreement. Blue and black arrows mark the bulk state at the center of the BZ and the Dirac cone, respectively. **b,** Same as **a,** except that DFT+DMFT results are superimposed on ARPES data. **c,** ARPES dispersion along A-R direction. Same as Fig. 1**i** or cut 3 in Fig. 1. The embedded DFT calculations deviate from ARPES data, especially near the A point (black arrow). **d,** Same as **c,** except that DFT+DMFT results are superimposed on ARPES data. The inclusion of Hund's coupling improves the agreement with ARPES.

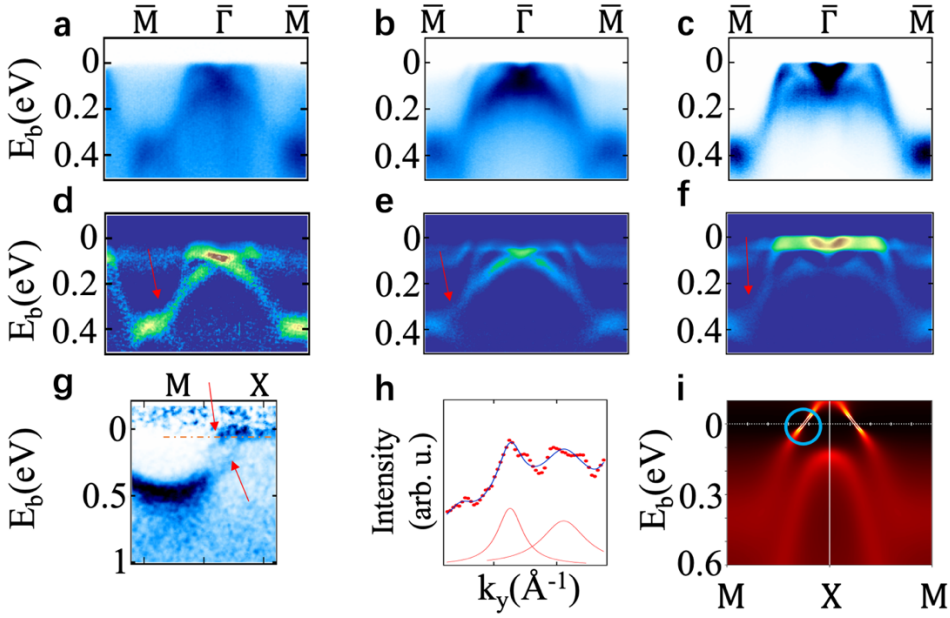

Supplementary Fig. 5. AFM nodal line along the A-M direction in YMn_2Ge_2. a-c, ARPES dispersion maps along the $\bar{M}$-$\bar{\Gamma}$ direction at various k_z positions, taken with incident photon energies of 140 (**a**), 107 (**b**), 97 eV (**c**), respectively. **d-f,** Corresponding second curvature plots of ARPES dispersion maps in **a-c**. The red arrows indicate the gapless fourfold Dirac crossings that remain along the A-M direction. **g,** ARPES dispersion along the M-X direction, taken with photon energy of 500 eV corresponding to the M-X-Γ high symmetry direction. Red arrows indicate the SOC split bands. **h,** Momentum distribution curve (MDC) through the orange dashed line in **g**. The blue line is the fit including two Lorentzians (shown as the red peaks) corresponding to the two SOC split bands. **i,** DFT+DMFT band structure along M-X-M direction. The blue circle indicates the SOC split bands. Therefore, the fourfold degenerate nodal line along the A-R direction is split into two branches along the X-M direction.

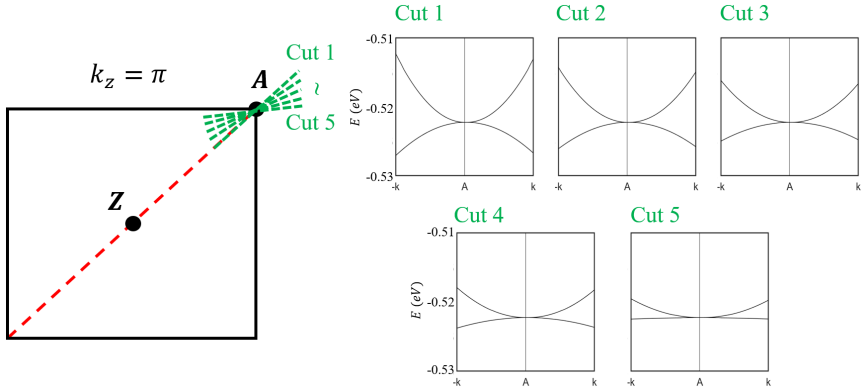

Supplementary Fig. 6. Quadratic band dispersions near the A point. Unlike the linear Dirac cone at R point, the Dirac crossing at A point displays a parabolic dispersion. Five cuts are extracted around A point, and all of them demonstrate a quadratic band crossing.

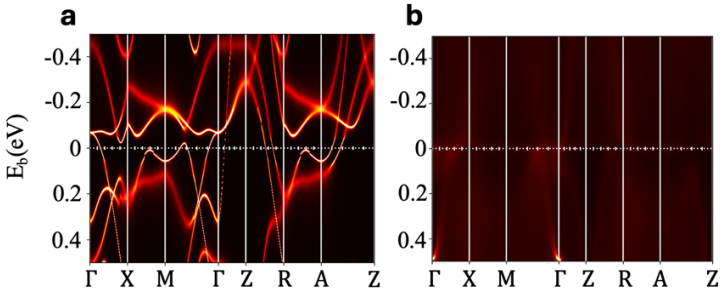

Supplementary Fig. 7. The hallmark of Hundness in YMn_2Ge_2. a-b, DFT+DMFT calculations of the paramagnetic electronic structure in YMn_2Ge_2. To study whether YMn_2Ge_2 is a Hund's metal or not, we set Hubbard U=5 eV and Hund's coupling J=0.1 eV (**a**) and 0.8 eV (**b**), respectively.

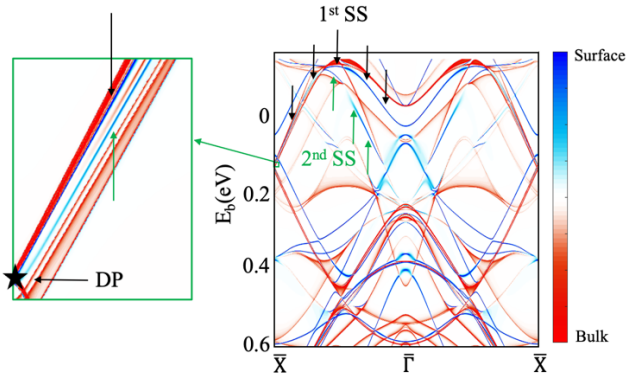

Supplementary Fig. 8. Drumhead surface state in YMn_2Ge_2. Semi-infinite surface calculations along the $\bar{X}$-$\bar{\Gamma}$-$\bar{X}$ high symmetry direction. Color bar indicates the surface state contribution. Black and green arrows mark the positions of the two drumhead surface states from the Dirac crossing. The left zoom in plot corresponds to the green box at the Dirac crossing. Black star represents the location of the Dirac point. Two surface states marked by the black and green arrows emerge from the bulk Dirac node.

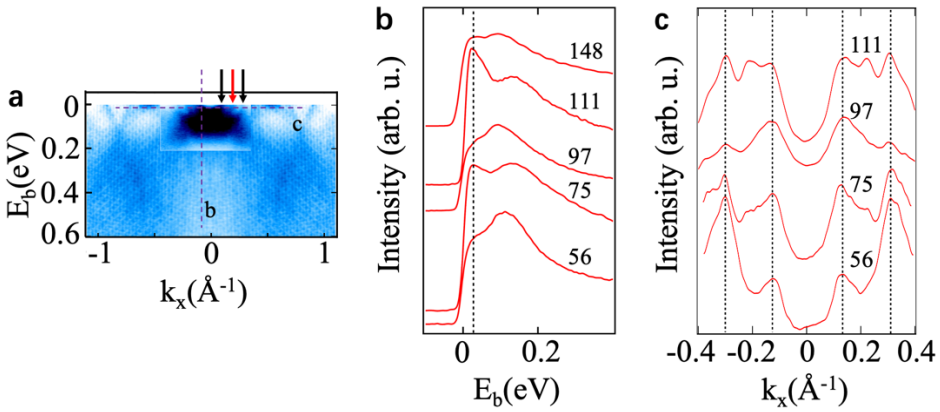

Supplementary Fig. 9. Photon energy scan of the drumhead surface state in YMn_2Ge_2. a, ARPES dispersion map along the R-Z-R high symmetry direction (same as Fig. 4**b**). **b,** Photon energy scan of an energy distribution curve (EDC) through the drumhead surface state marked by the vertical purple dashed line in **a**. Peaks highlighted by the black dashed line are the inner drumhead surface state (left black arrow in **a**) that displays no dispersion with photon energy, confirming its surface nature. As a comparison, the bulk state (second peak at higher binding energy in EDCs) corresponding to the red arrow in **a** shows a clear dispersion along the k_z direction. Incident photon energies are indicated as the black numbers. **c,** Photon energy scan of a momentum distribution curve (MDC) near the Fermi level marked by the horizontal purple dashed line in **a**. Peaks highlighted by the black dashed lines are the two drumhead surface states (black arrows in **a**) that don't change position in momentum space with photon energy, confirming their surface nature. Incident photon energies are indicated as the black numbers.

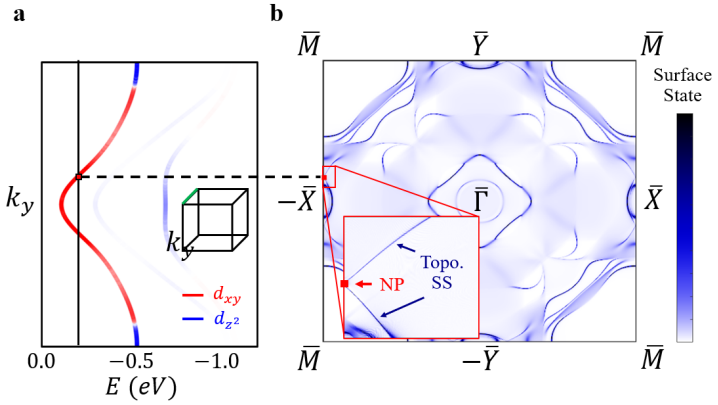

Supplementary Fig. 10. Drumhead surface state on the (001) surface. a, Dirac nodal line along the A-R direction. Same as Fig. 1**j**. Black vertical line denotes the binding energy of the constant energy contour in **b**. **b,** Constant energy contour integrated over all the k_z values on the (001) surface. The zoom-in plot displays the location of the Dirac crossing and the corresponding two drumhead surface states emerging from it.

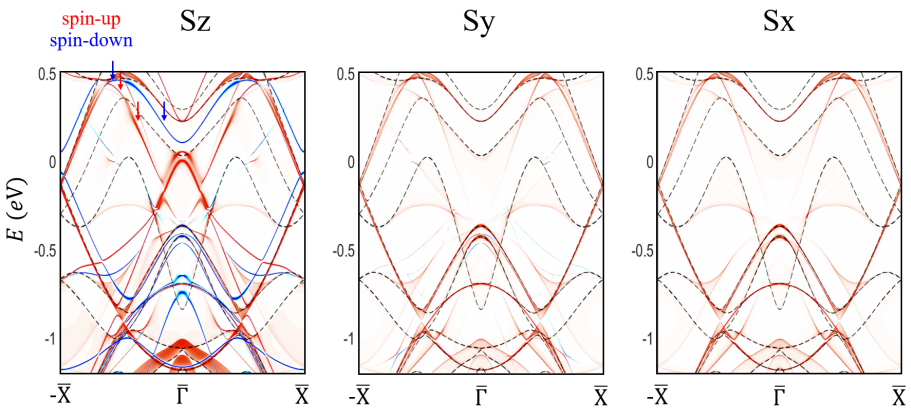

Supplementary Fig. 11. Spin polarization of the drumhead surface states. Spin polarization of the surface bands along the $\bar{X}$-$\bar{\Gamma}$-$\bar{X}$ high symmetry direction. The two drumhead surface states marked by the blue and red arrows display opposite S_z spin polarization and negligible polarization in S_x and S_y directions.

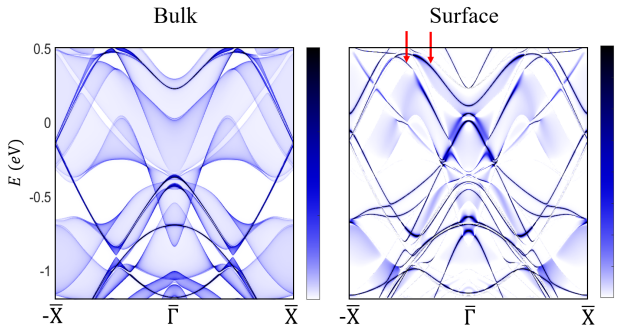

Supplementary Fig. 12. Semi-infinite surface calculations along the $\bar{X}$-$\bar{\Gamma}$-$\bar{X}$ high symmetry direction. Semi-infinite surface calculations excluding (left) and including (right) surface states along the $\bar{X}$-$\bar{\Gamma}$-$\bar{X}$ high symmetry direction. Red arrows mark the two drumhead surface states that only appear in the right panel.

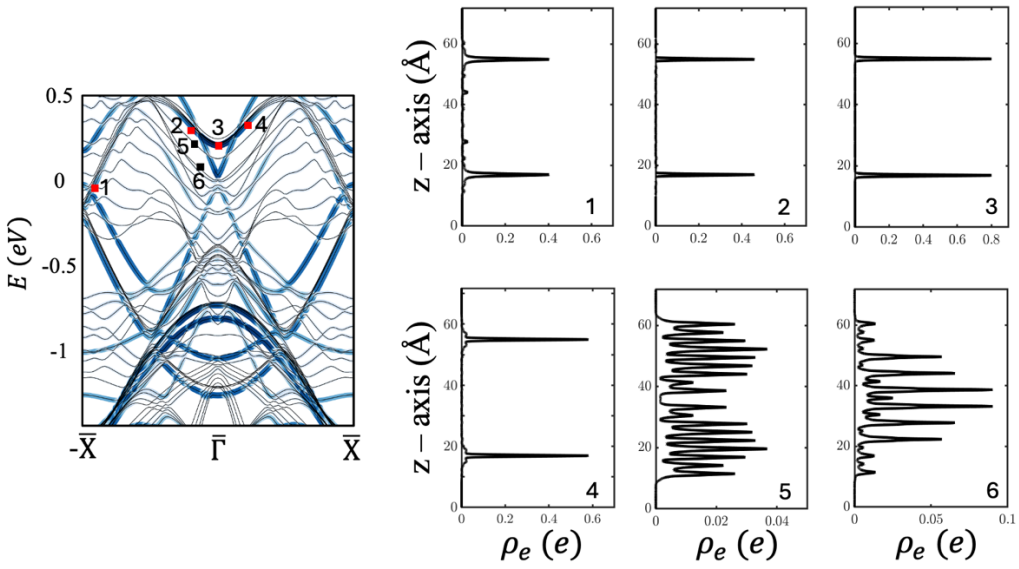

Supplementary Fig. 13. Charge density of selected points along the drumhead surface state and bulk states. Left: Finite-size slab calculations along the $\bar{X}$-$\bar{\Gamma}$-$\bar{X}$ high symmetry direction. Blue lines represent the intensity of surface states. Six points are selected. Points 1 to 4 are along the drumhead surface state and 5 to 6 are along bulk states. **Right**: Charge density of the points marked by the red and black squares in the left panel. Based on the charge density of points 1 to 4, the drumhead state is shown to be localized at the surface. As a comparison, the charge density of bulk states for points 5 and 6 shows an oscillatory behavior inside the bulk. Thus, the drumhead surface state has a surface origin.

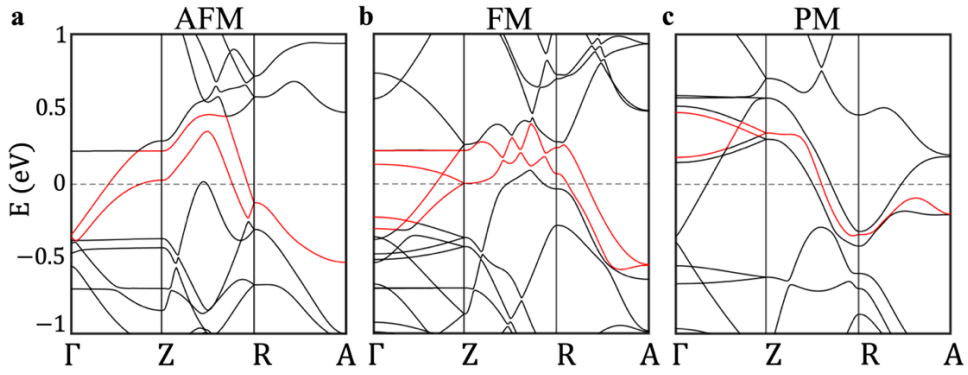

Supplementary Fig. 14. YMn_2Ge_2 band structures under different magnetization configurations. a, Antiferromagnetic. **b,** Ferromagnetic. **c,** Paramagnetic. Four bands are marked by red lines, indicating fourfold degeneracy in **a** along R-A direction leading to AFM Dirac nodal line on the boundary of the bulk BZ, twofold degeneracy in **b** along Z-R-A direction giving rise to a FM Weyl nodal surface on Z-R-A plane, and fourfold degeneracy in **c** along Z-R-A direction leading to a Dirac nodal surface on Z-R-A plane, respectively.

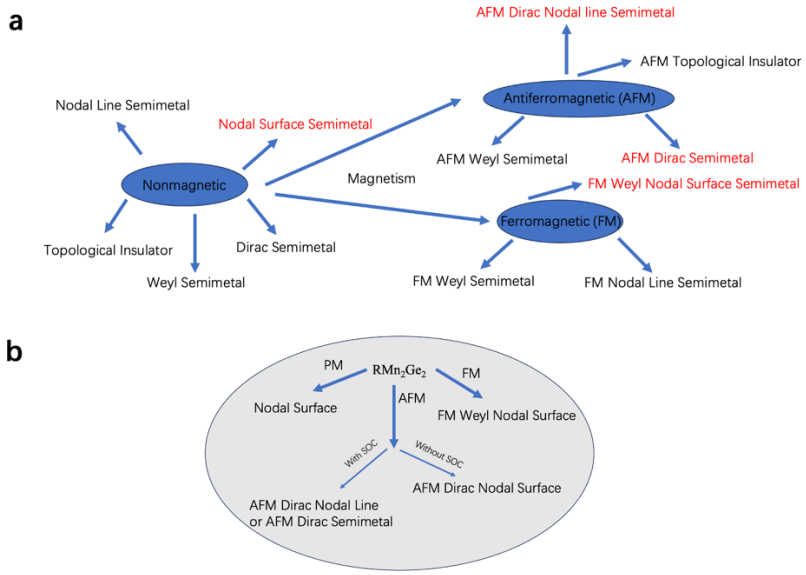

Supplementary Fig. 15. Novel topological phases in RMn_2Ge_2 (R=rare earth) family. a, Diagram showing various magnetic and nonmagnetic topological phases in condensed matter physics. Red topological phases have not been experimentally band-resolved but can be realized in YMn_2Ge_2 family. **b,** Diagram highlighting the various novel topological phases in YMn_2Ge_2 family.

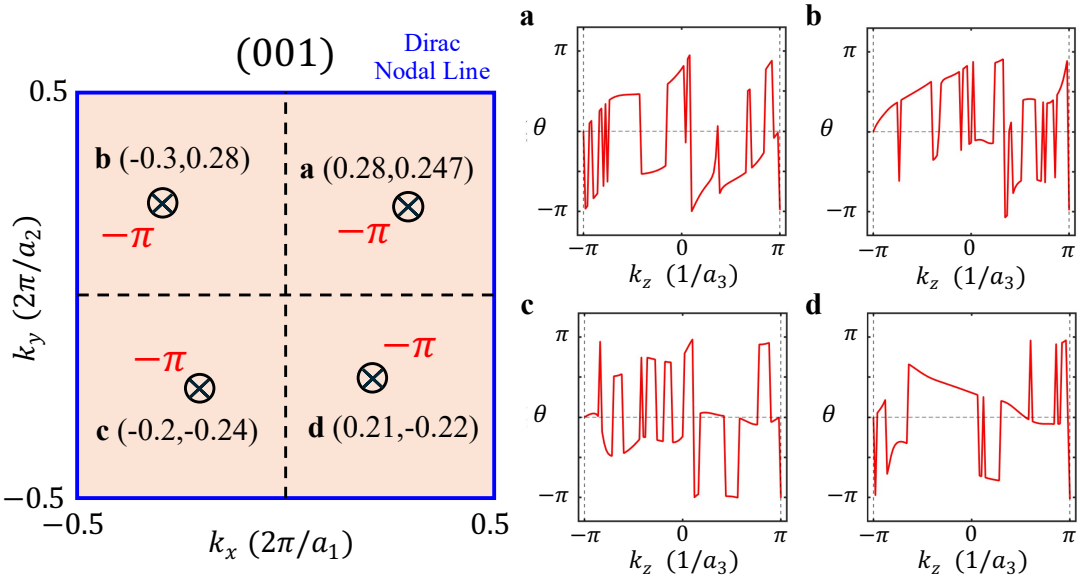

Supplementary Fig. 16. Schematic figure of the Zak phase by integrating k_z axis corresponding to (001) surface states. a-d, Wilson Loop along k_z axis for a-d points marked in the left panel. Since the Zak phase $\mathcal{Z}(k_x, k_y) = -\pi$ for any point on the $k_x - k_y$ plane, drumhead surface states are expected on the (001) surface in YMn_2Ge_2.

Mass enhancement/ Quasi-particle scattering rate	d_{z^2}	$d_{x^2-y^2}$	d_{xz} /d_{zy}	d_{xy}
U=5 J=0.1	1.26/2 meV	1.02/7 meV	1.37/2 meV	1.61/3 meV
U=5 J=0.8	4.80/215 meV	4.58/66 meV	6.39/476 meV	6.81/1337 meV

Supplementary Table 1. YMn_2Ge_2 as a Hund's metal. Quasi-particle mass enhancements and scattering rates for Mn *d* orbitals with different J values. When Hund's coupling (J) is increased, magnetic moment fluctuation increases dramatically. Moreover, the spectral function undergoes a coherent-to-incoherent transition (Supplementary Figs. 7**a-b**), with a large variation of *d*-orbital dependent quasi-particle mass enhancement and scattering rate. Therefore, our DFT+DMFT calculations clearly establish YMn_2Ge_2 as a Hund's metal.